PAPER

Check for updates

Preclinical validation of magnetic hyperthermia therapy for locally advanced oral cancer treatment

Priyadharshni Sriram,[a] Anjali Pandey,†[b] Aganiya Gopalakrishnan,†[b] Tina Mary George, [ID] [a] Nandish M.,[a] Sabbarinath Subramanian,[a] Rajesh Katoch*[a] and Shilpee Jain [ID] *[b]

Locally advanced tumors of the buccal cavity harbor abundant hypoxic and cancer stem cell populations, rendering them intrinsically resistant to conventional radiotherapy and chemotherapy. Current aggressive treatment regimens, though effective in part, often result in collateral tissue injury, functional impairment, and significant morbidity. Magnetic hyperthermia (MHT)—a minimally invasive technique that employs magnetic nanoparticles (MNPs) to generate localized heat under an alternating magnetic field (AMF)—represents a promising alternative, as its therapeutic efficacy is independent of tumor cell type or microenvironmental conditions. Despite extensive preclinical progress, clinical translation has been hindered by safety and feasibility challenges, particularly the reliance on non-translatable, high-frequency AMF systems. To address these hurdles, this study evaluated magnetic hyperthermia for oral squamous cell carcinoma (OSCC) using preclinical models and a scaled-up AMF generator designed within human safety thresholds, unlike prior studies that used non-translatable high-frequency fields. FDA-approved amino silane-coated Fe_3O_4 nanoparticles were synthesized *via* co-precipitation and confirmed to be pure and superparamagnetic ($M_s \sim 58$ emu g^{-1}) through XRD, FT-IR, and VSM studies. Three animal models were employed for preclinical validation: (i) a rat model for biodistribution and excretion studies as per ISO guidelines, (ii) a hamster model of OSCC induced by tobacco-related carcinogens, closely mimicking human oral cancer pathology, and (iii) a patient-derived xenograft (PDX) model to assess efficacy in large tumors. In rats, nanoparticles showed no systemic toxicity, were excreted *via* feces, and serum iron normalized within 72 hours. Hyperthermia treatment (2−5 cycles, ~45 °C) suppressed large tumor growth (>100 mm^3) and completely eradicated smaller tumors (<100 mm^3). A dose-dependent reduction in p53 staining confirmed the therapeutic efficacy and improved prognosis, underscoring the translational potential of magnetic hyperthermia in OSCC and other solid tumors.

Introduction

Oral cancer anatomy spans from the vermilion border of the lips to the circumvallate papillae of the tongue and the junction of the hard and soft palate.[1] Despite the possibility of self-assessment, early diagnosis, and easily accessible sites, the global epidemiological trends of oral cancer show a significant increase, with an overall five-year survival rate of 60%.[2] There is geographical heterogeneity in the prevalence of oral cancer, with higher rates in South and Southeast Asia, particularly in India, which accounts for about one-third of the total global burden.[3–5] Nearly 90% of these cases are squamous cell carcinoma (SCC), mainly caused by tobacco usage and alcohol consumption. Moreover, in the Asian population, the common habits of betel nut and tobacco chewing contribute to the highest global rates of oral cancer.[1]

Despite the emergence of newer technologies and therapies for cancer, and regardless of whether countries are developing or developed, the five-year survival rate has remained unchanged over the years.[5,6] Conventional treatment methods, such as surgery, radiation, chemotherapy, *etc.*, often fail to eliminate certain types of cells, such as hypoxic cells, cancer stem cells, and multi-drug-resistant cells, leading to a high recurrence rate. These resistant cells either evade binding to drug molecules or rapidly repair DNA damage to counteract the toxic effects of chemotherapy or radiation. As a result, survivors often experience a compromised quality of life even after undergoing aggressive treatment. Unavailability of biomarkers is also a major problem regarding the treatment of cancer. A suitable biomarker can detect and evaluate the cancer progression and the therapeutic effect of the chemotherapy drugs. Many types of cancer remain asymptomatic, and due to

ªMagHeals Private Limited, Bengaluru, India. E-mail: rajesh@magheals.com

ᵇSchool of Biosciences, Chanakya University, Devanahalli, Bengaluru, India. E-mail: shilpee.j@chanakyauniversity.edu.in

† Equal contribution.

lack of timely diagnosis, it gives cancer the opportunity to grow and spread all over the body before any medical intervention.[7]

Localized heat energy in the form of hyperthermia (ablation) therapy—where the temperature is raised to 40–45 °C (or above 45 °C for ablation)—can effectively target all types of cells, regardless of their cell cycle phase or mutations.[8,9] Technologies such as radiofrequency, microwave, and high-intensity focused ultrasound (HIFU) are available for this purpose.[10] However, some of these techniques are invasive and cannot be used for large areas or deeply seated tumors. For instance, radiofrequency and microwave ablation often require multiple electrodes to be inserted into the tumor, making them invasive. While HIFU is a non-invasive method, it cannot be used if the tumor is located near the bone.[11,12] Additionally, these techniques have limited penetration depth to target deeply seated tumors. Magnetic hyperthermia therapy can overcome most of these limitations.

In literature, extensive work has been reported for decades to understand the candidacy of magnetic hyperthermia therapy (MHT).[13–19] In this therapy, biocompatible magnetic nanoparticles are introduced into tumor tissue and by applying an alternating magnetic field (AMF), MHT generates localized heat capable of inducing cancer cell death with high spatial precision. This technique minimizes collateral tissue damage, enhances patient comfort, and can be synergistically combined with other therapies to overcome resistance mechanisms. Despite promising results, successful clinical translation of this therapy for solid tumors remains unachieved. Numerous nanoparticle-based delivery systems have shown high efficiency *in vitro* and *in vivo* studies,[20–22] yet clinical progress is limited due to inconsistent outcomes across study stages. For instance, MNP accumulation and retention vary with immune status and animal strain. Although several reports detail cellular-level particle uptake, most rely on immortalized macrophage cell lines, which lack physiological relevance and provide little insight into *in vivo* clearance. This disparity leads to inconclusive findings and hampers the clinical advancement of the therapy.[23–32] Furthermore, for most MHT applications, to prevent unintended tissue heating from field induced eddy currents, the Brezovich criterion defines a safe exposure threshold as $H \times f < 4.85 \times 10^8$ A ms^{-1}, where H is the magnetic field strength and f is the frequency.[33] Since the generation of heat by magnetic nanoparticles is more at higher frequencies, most hyperthermia experiments use frequencies above 200 kHz, which are unsuitable for human applications. Maier-Hauff *et al.* successfully demonstrated glioblastoma treatment at the clinical level using sub-threshold magnetic field intensity;[34,35] however, its use in oral cancer is still remain unexplored. To bridge this gap, we conducted preclinical studies in relevant oral cancer models to evaluate the therapy's safety and efficacy and advance clinical translation.

In this study, we specifically assessed aminosilane (APTES)-coated biocompatible Fe_3O_4 nanoparticles (AS-IONPs) as candidates for magnetic hyperthermia therapy. The choice of APTES is supported by its prior regulatory approval and superior cellular retention in cancer cells compared to other coatings. Silica-based coatings are chemically inert and minimize magnetic dipolar interactions, enhancing colloidal stability. APTES uniquely provides both Si and NH_2 functionalities which enables versatile biomolecule conjugation. In aqueous conditions, it hydrolyses to form silanol groups that condense with surface metal hydroxyls on the nanoparticles.[36–39]

Results

Motivated by the potential translation of magnetic hyperthermia therapy, we designed a biocompatible and stable suspension of magnetic iron oxide nanoparticles (IONPs). The magnetic IONPs (Fe_3O_4) were synthesized *via* the coprecipitation method, with a size of approximately 11.3 nm as confirmed by TEM (Fig. 1a). However, in aqueous suspension, these bare (uncoated) IONPs tended to agglomerate due to high surface energies[37] or the presence of a solvation shell and counter-ion layer, which inflates the apparent hydrodynamic radius, as shown by dynamic light scattering (DLS) analysis.[40]

DLS measurements of the uncoated IONPs yielded an effective diameter of ~230 nm with a moderate polydispersity index (0.129). The intensity-weighted distribution showed a single peak centered at ~230 nm, reflecting the dominant scattering contribution from this population. Conversion to a volume-weighted distribution retained the peak at ~230 nm. Fig. 1e shows the AS-IONPs suspension had a mean hydrodynamic size of ~112 nm and a narrow size distribution, as evidenced by a low polydispersity index (PDI ~0.15) which is further supported by the TEM image (Fig. 1c).

Fig. 2a shows the XRD patterns for coated and uncoated nanoparticles to demonstrate the phase purity and expected peak positions. Due to high surface to volume ratio, Fe_3O_4 (magnetite) IONPs have a propensity for oxidation at the surface and oxidation to γ-Fe_2O_3 (maghemite).[41] Both Fe_3O_4 and γ-Fe_2O_3 have similar cubic spinel structure and almost identical lattice constants (Fe_3O_4 = 8.396 Å; γ-Fe_2O_3 = 8.351 Å). This results in a very similar X-ray diffraction pattern with a slight
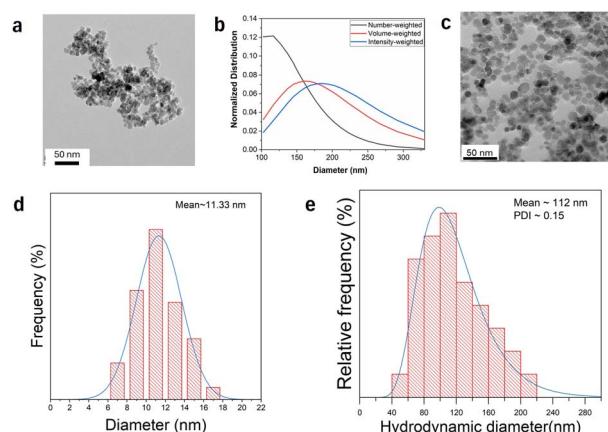

Fig. 1 Iron oxide nanoparticles (IONPs) (a) TEM image of uncoated IONPs, (b) DLS number- and volume-weighted distributions for the uncoated IONPs, (c) TEM image of AS-IONPs, (d) particle size distribution of uncoated NPs, and (e) hydrodynamic particle size distribution of AS-IONPs.
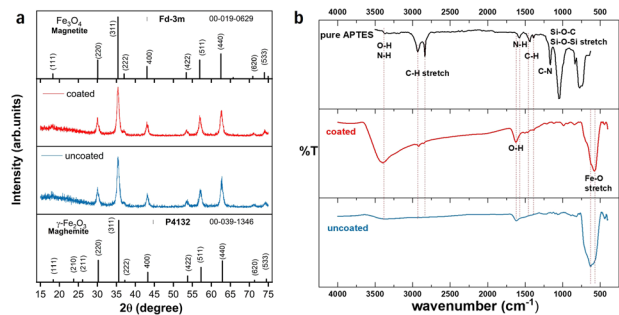
Fig. 2 (a) XRD spectra of uncoated and coated IONPs (b) FTIR spectra of uncoated and coated IONPs. A reference spectrum of pure APTES has been reproduced from ref. 42.

shift (0.05–0.5°) of peaks to right in maghemite owing to smaller lattice constant. Thus, it is very difficult to distinguish between them on the basis of XRD alone. The observed XRD spectra have been indexed to standard reference patterns for cubic Fe_3O_4 with $Fd\bar{3}m$ space group (ICDD No. 00-019-0629) and γ-Fe_2O_3, with cubic $P4_132$ space group symmetry (ICDD No. 00-039-1346). The absence of impurity or secondary peaks confirms the phase purity. No additional peaks beyond the Fe_3O_4/γ-Fe_2O_3 patterns were observed, suggesting the amorphous nature of the polymer coating. Using the Debye–Scherrer equation, the mean crystallite size was determined to be approximately 11.3 nm.

Fourier transform infrared spectroscopy (FTIR) was utilized to evaluate the chemical nature of the nanoparticles. Fig. 2b shows the FTIR spectrum of the coated AS-IONPs and uncoated IONPs along with a reference APTES spectrum. In the experimental range of 400–4500 cm^{-1}, Fe_3O_4 shows an intense absorption band at 570–580 cm^{-1} which is assigned to the Fe–O stretching motion of the tetrahedral and octahedral sites.[43] Aminosilane (APTES) on the other hand is a silane coupling agent with both an amino (–NH_2) group and hydrolysable alkoxy silyl groups. Its characteristic IR absorption spectra arises from N–H stretching (3400–3250 cm^{-1}), C–H stretching (2930 & 2860 cm^{-1}), N–H bending deformation (1650–1580 cm^{-1}), C–N stretching (1220–1020 cm^{-1}), Si–O–C stretching (1100–1080 cm^{-1}), Si–C stretching (800–850 cm^{-1}), with Si–O–C band

being an excellent marker of pure APTES.[42] In the observed FTIR spectra (Fig. 2b), the 3430 cm^{-1} and 1630 cm^{-1} absorption peaks correspond to the stretching and bending modes of adsorbed water molecules (O–H) on the nanoparticles surface. However, the peaks due to the stretching and bending bond of the terminal amine group (–NH_2) on the coated nanoparticles cannot be clearly distinguished due to overlap with the O–H peaks. The sharp peaks of the alkyl (C–H) group are observed at 2937 cm^{-1} and 2840 cm^{-1} in the aminosilane coated samples and absent in uncoated samples. C–H bending and C–N stretching mode peaks are visible around 1380 cm^{-1} and 1170 cm^{-1} respectively. Likewise, the peaks between 1100–1000 cm^{-1} indicate the establishment of Si–O–Si and Si–O–C networks on nanoparticles. These features are notably absent in the uncoated samples. The zeta potential of the coated IONPs suspension, measured at approximately +40 mV, further confirms that they possess a sufficiently stable surface coating. Intense Fe–O absorption bands are present between 650–550 cm^{-1}. For uncoated samples, broad absorption band is visible with an intense peak centred at ~630 cm^{-1}, indicating the presence of γ-Fe_2O_3.[44] In comparison, the band is narrower for aminosilane coated samples, indicating comparatively fewer defects. Different peak assignments and their wavenumbers are provided in Table 1.

Fig. 3a shows the magnetic hysteresis curves of the nanoparticles in the field (H) range of 0–2 T. As the magnetic field increases, the magnetization initially increases linearly, typical of paramagnetic materials. With further increase in the magnetic field, the slope of the M–H curve decreases, and the magnetization saturates (M_s), showing no significant change beyond this point. The narrow 'S'-shaped hysteresis loops with high magnetization and low coercivity are characteristic of superparamagnetic materials. The M_s values for uncoated and coated IONPs are 57 emu g^{-1} and 70 emu g^{-1}, respectively. The inset of Fig. 3a shows the area enclosed under the M–H loop in the linear region, providing a coercivity (H_c) of approximately 14 gauss for the nanoparticles. The large M_s, low coercivity, and negligible remanent magnetization (M_r)~1.4 emu g^{-1} for AS-IONPs and ~1.2 emu g^{-1} for uncoated IONPs, indicate that the nanoparticles are single domain and superparamagnetic in nature.

Table 1 FTIR spectra peak assignments and their wavenumbers

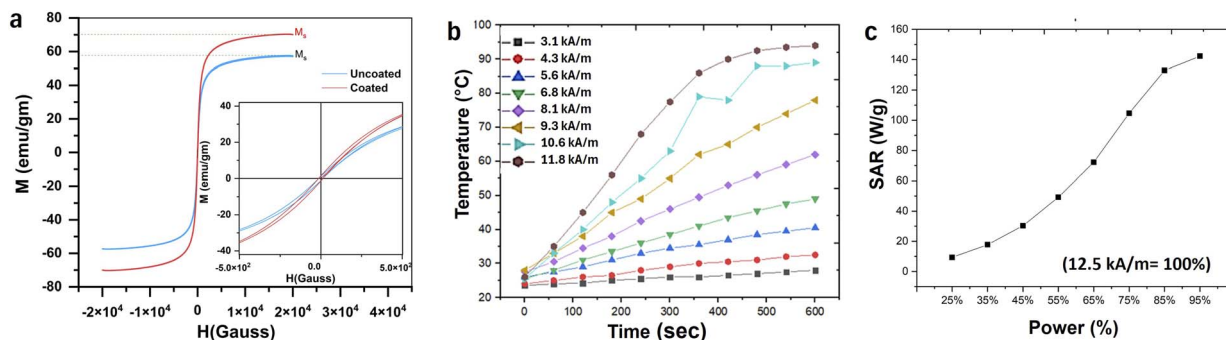| Assignment (mode)	Wavenumber (cm^{-1})	References
N–H stretching, primary amine	~3500–3300	45
O–H stretching	~3435	46
C–H asymmetric stretching	~2970–2930	42
C–H symmetric stretching	~2870–2800	
O–H bending	~1630	46
NH_2 deformation (scissor)	~1600–1500	42
C–H bending	~1500–1300	
C–N stretching	~1220–1020	
Si–O–C	~1100–1080	
Si–O–Si	~1100–1000	
Fe–O stretching	~590–570 – Fe_3O_4	43
	~630, 590 and 430 γ-Fe_2O_3	

Fig. 3 (a) Hysteresis (M–H) curves of coated and uncoated IONPs. (b) Variation in suspension temperature with time under an external alternating magnetic field (AMF; 100 kHz, 0–12 kA m^{-1}). The temperature change was recorded using an optical fiber-based thermometer. (c) Specific absorption rate (SAR) of the AS-IONPs suspension at different AMF intensities (12.5 kA m^{-1} = 100%).

Further, alternating magnetic field (AMF) heating efficacy of the nanoparticle suspension was evaluated using an in-house AMF generator, operating at a frequency of 100 kHz and a magnetic field intensity ranging from 0 to 12.5 kA m^{-1}. The power of the AMF is automatically tuned with a real time feedback loop to prevent overheating. Temperature measurements were recorded using a fibre optic thermometer. Fig. 3b shows the temperature rise of the suspension as a function of the magnetic field intensity/power. It obtained within a few minutes. The specific absorption ratio (SAR) of the AS-IONPs was determined to be ~140 W g^{-1} at highest field intensity as shown in Fig. 3c.

The initial cytocompatibility of the AS-IONPs was evaluated *in vitro* using the SCC-25 cell line, a squamous cell carcinoma cell-line derived from a male patient using MTT assay.[47] Fig. 4a (Trypan blue assay in Fig. S2) shows the cell viability after incubation with AS-IONPs for different time intervals. Preliminary *in vitro* viability studies with HeLa and L929 cell lines confirmed that up to 1 mg mL^{-1} concentrations of AS-IONPs are biocompatible and do not affect cell viability (Fig. S1). For efficient therapeutic outcomes, it is essential to have a minimum of 10^5 nanoparticles per cell to generate sufficient heat for achieving the target temperature.[48] Thus, for the SCC-25 cell line, a higher concentration (~10^{10} NPs per cell) was used to assess cell viability. Interestingly, Fig. 4a shows that while the initial incubation period (24 and 48 hours) results in significantly reduced viability compared to the control, cell viability at concentrations up to 2 mg mL^{-1} was found to be comparable to

the control. Furthermore, the cellular morphology was analyzed using a fluorescence microscope to observe the effect of various concentrations of nanoparticles on the cells. Fig. 4b confirms that AS-IONP concentrations up to 6 mg mL^{-1} did not alter cellular morphology as compared to control; however, at higher concentrations, the cytoskeleton and nucleus of most cells appeared distorted.

For clinical translation, identifying the maximum tolerated safe dose of the nanoparticle suspension is crucial. Accordingly, two solid weight concentrations of AS-IONPs suspension— 150 mg mL^{-1} and 300 mg mL^{-1}—corresponding to 150 mg kg^{-1} and 300 mg per kg body weight of rats, respectively, were selected for organ biodistribution studies. ICP-MS analysis confirmed that about 80% of the solid weight content comprised elemental iron.

Histopathological analysis of major organs (liver, kidney, spleen, heart, and lungs) after 72 hours of AS-IONP administration revealed no morphological differences compared to control (Fig. 5a). No accumulation of nanoparticles was observed in any of the organs. Biochemical analysis (Fig. S2) further confirmed that there was no loss of organ function, even after administration of higher doses of AS-IONPs. ICP-MS analysis also showed that the majority of the injected AS-IONPs were eliminated from the body through feces, with minimal excretion through urine.

Fig. 5b shows the serum iron levels, as determined by ICP-MS, at different time intervals (0, 0.5, 4, 6, 24, 48, and 72 hours) post-dosing in Wistar rats. Serum iron levels initially
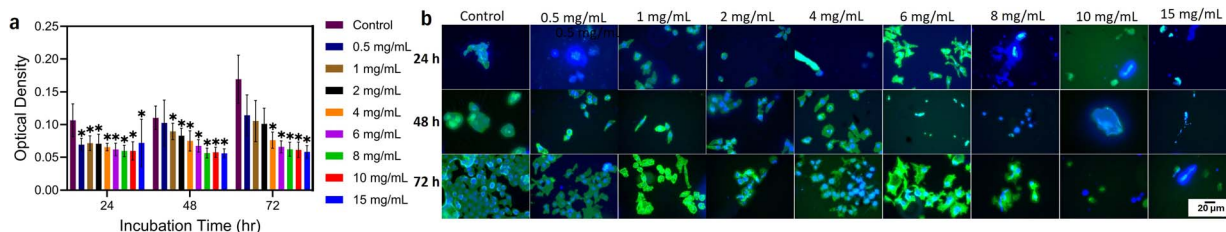

Fig. 4 (a) MTT viability assay of SCC-25 cells after incubation with various concentrations of AS-IONPs for different time intervals. Results are expressed as mean ± SD. Asterisk indicates $P \leq 0.05$ statistical significance compared with the untreated control. (b) Fluorescence microscopy images of SCC-25 cells after incubation with various concentrations of AS-IONPs. Green fluorescence represents actin filaments, and blue indicates cell nuclei.
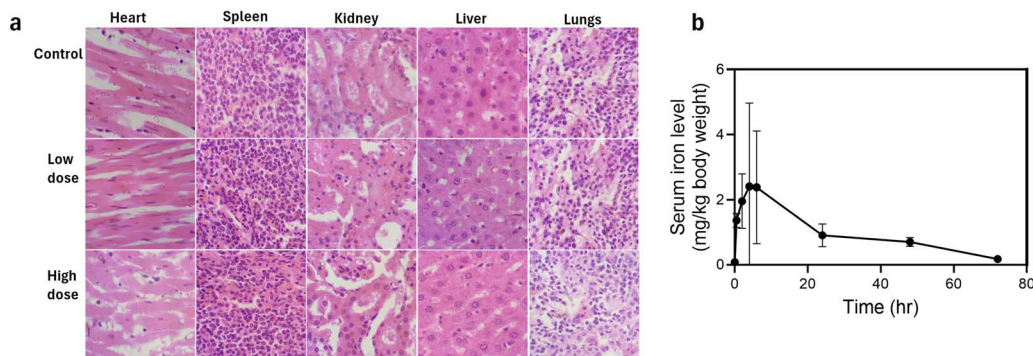
Fig. 5 (a) Histopathology images of various organs after 72 hours of administration of AS- IONPs to rats-control (w/o AS-IONPs), low dose (150 mg per kg body weight), and high dose (300 mg per kg body weight) [100× magnification], (b) depicts the serum iron levels with respect to time.

increased up to 6 hours, then gradually decreased, returning to normal values by 72 hours post-injection. The analysed haematology parameters of rats at all dose levels (150 mg kg^{-1} and 300 mg per kg body weight) were observed to be comparable with the control group. No significant changes were observed in HGB, HCT, MCV, MCH, MCHC, RBC, WBC, platelet count and differential count value in rats at all dose levels (150 mg kg^{-1} and 300 mg per kg body weight), and were found to be comparable with the control group. The summary of haematology parameters of all rats are presented in Fig. S3.

Transmission electron microscopy (TEM) was employed to investigate the fate of nanoparticles eliminated through faeces (Fig. 6). It revealed that the size of the eliminated nanoparticles was identical to that of the original formulation that was administered. Elemental mapping using energy-dispersive X-ray spectroscopy (EDS) showed the presence of iron, silicon, nitrogen, carbon, and oxygen, confirming the successful coating of the nanoparticles (Table 2), this further confirmed that the coating remained intact, as all elements of the coating could be mapped across the nanoparticle volume. In contrast, nanoparticles excreted in urine appeared to have disrupted coatings, resulting in agglomeration of the particles compared to the more uniform particle distribution observed in faeces samples.

These findings strongly suggest that the coating remains stable in the physiological environment, effectively inactivating the nanoparticles during their residence in the body. We conducted preliminary studies to assess the efficacy of magnetic hyperthermia in killing tumor cells and enhancing survival. AS-IONPs suspension (solid weight content 150 mg mL^{-1}) were injected directly into the chemically induced tumors in the buccal pouch of Syrian hamsters. CT scan studies demonstrated significant dwell time of the nanoparticles in the tumor tissue (Fig. 7a and b). The tumors injected with AS-IONPs were subjected to an AMF of 100 kHz and a magnetic field intensity between 2 and 10 kA m^{-1} to maintain a temperature of around ~44 °C for 30 minutes. The AS-IONPs remained at the tumor site for up to six weeks if exposed to alternating magnetic field (AMF) exposure, with no significant reduction in the volume of the nanoparticle agglomerate (Fig. 7b). In contrast, without magnetic field exposure, the nanoparticles were cleared from the site after the sixth day of injection (Fig. 7a). Two hyperthermia treatment sessions were administered to all the treatment groups. Fig. 7c shows significant inflammation and necrosis of the tumor tissue on the fourth and ninth day, respectively. The necrotic tissue cleared, leading to a substantial reduction in tumor volume by the eleventh day (Fig. 7c). Treated animals demonstrated significant tumor shrinkage or complete elimination, along with improved survival (Fig. 7d).

The efficacy study was also conducted in a xenograft nude mouse model, since in the hamster carcinogen model, the
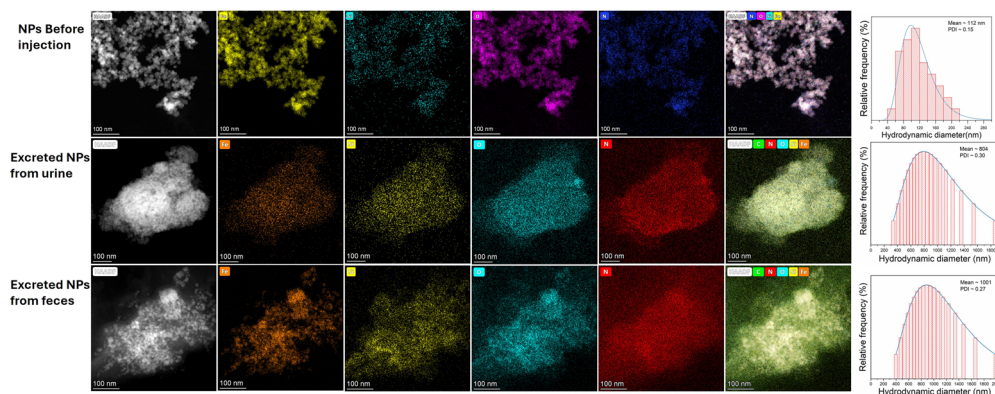

Fig. 6 TEM images and elemental mapping of excreted AS-IONPs from feces and urine of rats after 24 h of injection.

© 2025 The Author(s). Published by the Royal Society of Chemistry

Table 2 Approximate weight % for selected elements

Elements	Urine	Feces
Fe	2.1%	4.9%
Si	4.4%	3.6%
O	65.1%	49.8%
N	28.4%	41.7%

maximum tumor size achieved was small (<20 mm^3). To evaluate the effectiveness of hyperthermia treatment for tumors larger than 1 cm^3 and to replicate the human tumor microenvironment, we selected the xenograft nude mouse model. Once the tumors reached approximately 100 mm^3, magnetic hyperthermia treatment was initiated. Fig. 8a shows an image of the scaled-up in-house AMF generator, including the working coil in which the animals were placed during treatment. Tumor temperatures were monitored using a fiber optic thermometer inserted directly into the tumor. CT scan images revealed that without AMF application; the AS-IONPs cleared from the injection site. However, unlike in hamsters—where all NPs cleared completely—the nude mice retained some agglomerated particles at the tumor periphery even after one week without AMF exposure. Conversely, when AMF was applied, retention of NPs at the tumor site was observed (Fig. 8c and d). Because the IONPs persisted at the tumor site for an extended period, no additional injections were performed in subsequent treatment sessions for any group.

During the treatment, the intratumoral temperature was recorded using a fiber-optic thermometer inserted into the tumor through a 24-gauge cannula, as shown in Fig. 8a. The temperature at the site was maintained between 42 °C and 46 °C Fig. 8b. Fig. 8e illustrates the progression of tumor volume over time for various treatment regimens. In the control group, tumor volume increased steadily, representing natural tumor progression. Similar trends were seen in groups treated with IONPs alone or AMF alone, indicating that neither component alone provided therapeutic benefit. A single combined treatment session produced mildly slowed tumor growth. Seven
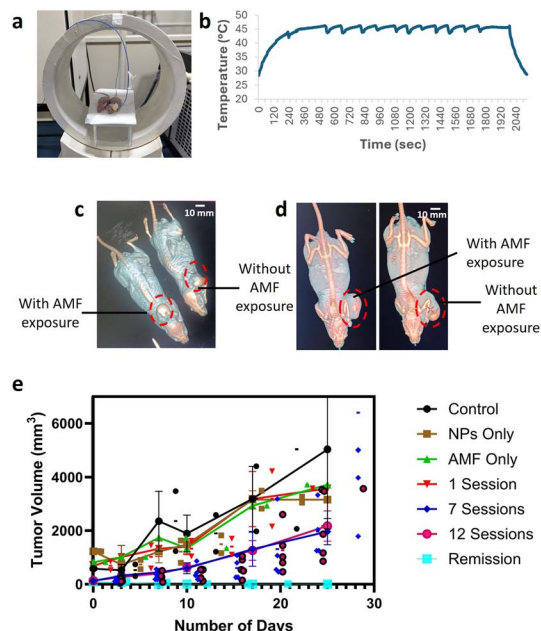

Fig. 8 (a) Photograph showing the alternating magnetic field (AMF) generator (100 kHz and 0–12 kA m^{-1} varying field) and the intratumoral insertion of an optical fiber-based thermometer using a cannula for temperature monitoring. (b) The temperature profile maintained during the treatment. CT scan images of nude mice showing the tumor site after (c) one day and (d) three weeks of AS-IONPs (100–150 μL of 150 mg mL^{-1}) instillation at the site. In both of these images, on the left side is an animal after exposure to AMF (100 kHz and 0–12 kA m^{-1} varying field) and on the right side is an animal without AMF exposure, and (e) time-course of tumor volume changes in control and treated groups measured at indicated time points. Data are presented as mean ± SEM, and individual animal data points are overlaid to illustrate variability within each group. Statistical analysis was performed using two-way ANOVA followed by Tukey's multiple comparisons test ($p \leq 0.05$ considered significant).

treatment sessions resulted in a moderate reduction in tumor growth rate. Notably, animals that received twelve treatment sessions exhibited substantial tumor suppression, with tumor volume significantly lower than in groups with fewer sessions. In one of the groups where treatment started once tumor size reached about 100 mm^3, the tumor disappeared completely after 5 sessions of hyperthermia @ 45 °C indicating a robust therapeutic response and potential for long-term tumor control. Additionally, p53 expression patterns varied distinctly across the treatment groups (Fig. 9). Reference control tissues showed no nuclear staining, indicating normal p53 expression. Control tumors and IONPs-only samples showed moderate expression (3+). The AMF-only group, representing untreated tumors, showed intense and widespread nuclear staining in nearly all tumor cells, indicative of strong p53 overexpression often linked to TP53 mutation and aggressive tumor behavior. Strikingly, all treated groups showed a marked reduction in p53 staining. Most treated tissues displayed only mild (2+) or focal (1+) staining, with no samples showing the intense expression seen in the AMF-only group. This reduction suggests that the hyperthermia treatment effectively modulated tumor behavior and reduced abnormal p53 accumulation.[49,50]
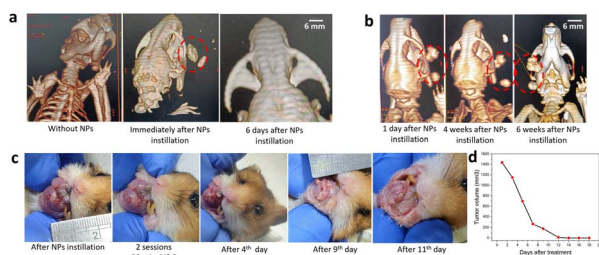

Fig. 7 CT scan images of hamsters before and after intratumoral instillation of AS-IONPs: (a) without AMF exposure and (b) with AMF exposure (100 kHz and 0–12 kA m^{-1} varying field). The red dashed circle indicates the injection site (100–150 μL of 150 mg per mL AS-IONPs). (c) Representative photographs showing oral tumor regression during the treatment period. The intratumoral temperature was monitored using an optical fiber-based thermometer introduced through a cannula. (d) Treatment response curve showing reduction in tumor volume over time.
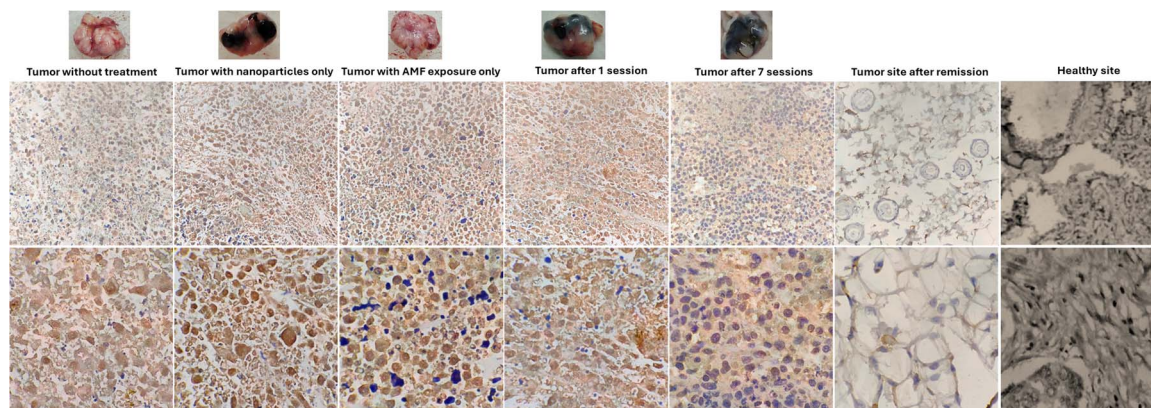
Fig. 9 Immunohistochemistry analysis of p53 expression in tumor tissues (inset: dissected tumor chunks) (top panel at 40× and bottom panel at 100×).

Discussion

The superparamagnetic amino silane coated iron oxide nanoparticles (AS-IONPs) were successfully synthesized using the co-precipitation method under a nitrogen atmosphere, which helped in forming stable and phase-pure Fe_3O_4 nanoparticles suitable for biomedical use. DLS measurements of the uncoated IONPs yielded an effective diameter of ~230 nm with a moderate polydispersity index (0.129). The intensity-weighted distribution showed a single peak centered at ~230 nm, reflecting the dominant scattering contribution from this population. Conversion to a volume-weighted distribution retained the peak at ~230 nm, confirming the unimodal nature of the dispersion. The number-weighted distribution also exhibited the same peak but with a slightly broader shape, consistent with the presence of smaller particles contributing proportionally more in number but less in volume or intensity. The overlap of all three distributions indicates that the IONPs are essentially monomodal without significant large-scale aggregation. To stabilize the nanoparticle suspension, aminosilane (APTES) coating was applied, which significantly reduced the agglomeration of Fe_3O_4 nanoparticles (AS-IONPs) by providing a steric and electrostatic barrier through the formation of a silica network and surface amino groups, thereby enhancing colloidal stability. The zeta potential of uncoated IONPs was +2.45 mV, which increased to +40 mV after the APTES coating.

Initial uncoated IONPs purification was carried out through magnetic separation, and after coating dialysis, which helped remove impurities and improve the stability of the particles in suspension. XRD analysis confirmed that the particles had a crystalline magnetite structure with no impurity peaks, showing that their structure remained stable (Fig. 2a). TEM images revealed that the particles were mostly spherical and monodisperse with size averaging around 11.33 nm (Fig. 1a and b). Elemental mapping using EDS showed the presence of iron, silicon, nitrogen, carbon, and oxygen, confirming that the particles were successfully coated. Another important parameter for AS-IONPs suspension is the hydrodynamic diameter as it determines the clearance pathway of the nanoparticles from the bloodstream. Smaller particle size enhances accumulation and diffusion in the tissue, whereas larger particles are rapidly cleared through liver and spleen. Interestingly, TEM images of fecal samples after excretion showed that the particles maintained their size and coating, proving that they were stable even in biological conditions (Fig. 6). Altogether, the study demonstrates that these AS-IONPs are uniform, magnetically responsive, and remain stable in biological environments, making them useful for medical applications such as imaging, targeted therapy, and magnetic hyperthermia.[51] While XRD and TEM studies suggest formation of stable AS-IONPs, FTIR clearly established the role of aminosilane coating in preventing surface oxidation and formation of polymorphic γ-Fe_2O_3, which remains ambiguous from structural studies as both polymorphs have identical crystal structure. Fe oxidation state is higher in γ-Fe_2O_3 (+3) compared to mixed (+2, +3) in Fe_3O_4. This subtle difference in oxidation state, is however distinguishable in FTIR absorption spectra.[43] When narrow, it suggests the high purity and crystallinity of the sample. However, in the presence of defects and secondary phases, like in the case of γ-Fe_2O_3 which is considered to be a defective form of magnetite, the Fe–O absorption band becomes broader and additional modes are expected at 630, 590 and 430 cm^{-1}.[44] The preservation of surface stoichiometry in AS-IONPs is reflected in their superior magnetic performance. Interestingly, the AS-IONPs show higher saturation magnetization (M_s: 70 emu g^{-1}) than bare ones (57 emu g^{-1}), which appears counterintuitive since nonmagnetic coatings usually dilute the magnetic response. However, this enhancement can be explained by the coating's role in preventing surface oxidation and preserving magnetic order. The magnetic behavior of Fe_3O_4 IONPs depends on particle size, surface effects, anisotropy, and crystallinity—all influenced by synthesis methods. Below 10–20 nm, Fe_3O_4 exhibits superparamagnetism with zero remanence (M_r), while high surface-to-volume ratios induce surface spin disorder and reduce M_s. Additionally, oxidation of Fe^{2+} to Fe^{3+} and formation of maghemite (α-Fe_2O_3) or hematite (α-Fe_2O_3) degrade crystallinity and lower M_s from 60–80 emu g^{-1} (magnetite) to 50–70 emu g^{-1} (maghemite).[41] Surface oxidation and agglomeration thus pose

major challenges to magnetic stability. Surface coatings mitigate these effects by protecting the core and stabilizing magnetic spins. Typically, nonmagnetic coatings such as PEG, PVA, dextran, or SiO_2 reduce M_s because they contribute mass without magnetism-e.g., PEG- and SiO_2-coated Fe_3O_4 show M_s of 58.9 and 45.6 emu g^{-1} versus 74.9 emu g^{-1} for uncoated IONPs.[52] Yet, in some cases, coatings like PEG or APTES enhance M_s by preventing oxidation, maintaining Fe^{2+} content, and retaining superparamagnetic behavior.[53] The coating chemistry critically determines oxidation resistance, crystallinity, and spin alignment. Comparative studies report that APTES and citrate coatings more effectively preserve magnetite phases, achieving M_s values around 80 emu g^{-1}—significantly higher than dextran-coated IONPs (∼70 emu g^{-1}).[54] Overall, APTES serves as an optimal coating by forming strong Si–O–Fe bonds, reducing oxidation, enhancing colloidal stability, and maintaining ordered surface spins, thereby maximizing the magnetic efficiency of Fe_3O_4 nanoparticles for biomedical and hyperthermia applications.

One of the key parameters for use of AS-IONPs in MHT is their SAR value. Specific Absorption Rate (SAR) is the measure of the rate at which magnetic nanoparticles (MNPs) convert electromagnetic energy into heat. SAR is crucial for effective MHT, as higher values enable tumors to reach therapeutic temperatures efficiently. It guides nanoparticle dosing, ensures controlled & safe heating. It also aids treatment planning by predicting thermal responses in vivo, making it a key parameter for safe and effective hyperthermia therapy. Furthermore, the SAR depends on the distribution of individual nanoparticles IONPs), as well as the external magnetic field intensity and frequency.[55] One of the reasons for the delay in translating this therapy to clinical settings is that commercially available AMF generators typically use high frequencies above 200 kHz to achieve high SAR of IONPs which are not suitable for human application.[22,56] Therefore, the high SAR value (140 W g^{-1}) reached @ 100 kHz in the present work, and is a significant step towards clinical translation of MHT.

For safety and efficacy studies, relevant cell and animal models have been chosen to closely mimic the human oral cancer microenvironment. As discussed earlier, for toxicity evaluation in vitro, SCC-25 cells were exposed to very high concentrations (∼10^{10} IONPs per cell).[57] At these concentrations, the nanoparticles inhibited cell division, as indicated by stagnant optical density values. However, the cells remained viable, showing no significant reduction in numbers after 72 hours compared to the control group. This observation correlates with the cellular morphologies of SCC-25 cells shown in Fig. 4b. As evident from Fig. 4b, within 24 hours after seeding, a high number of AS-IONPs were associated with individual cells, leading to altered cellular morphology at concentrations above 6 mg mL^{-1}. As the cell density increased over time, cellular morphology appeared normal at 8 mg mL^{-1}; however, at 10 mg mL^{-1} and higher concentrations, the cells again exhibited unhealthy morphology. These results suggest that cells were not completely damaged at higher concentrations. Instead, the transient growth arrest observed was likely due to morphological alterations, which appeared to be reversible over

time. Biodistribution and clearance studies in Wistar rats demonstrated that the AS-IONPs did not accumulate in organs (Fig. 5a) and were primarily excreted via faeces, with the coating remaining intact (Fig. 6), indicating minimal systemic interaction and reduced risk of adverse effects. No morbidity or mortality was observed in animals administered IONPs at doses of 150 mg kg^{-1} and 300 mg kg^{-1}, and no treatment-related clinical signs were noted. Liver and kidney function, assessed through serum biochemical and hematological analyses, remained normal in treated groups relative to controls (Fig. S2). Bodyweight in treated animals was comparable to controls, further indicating the nanoparticles were non-toxic. Overall, these results confirm that the coated AS-IONPs are biocompatible, non-toxic, and safely cleared from the body, supporting their suitability for therapeutic applications like magnetic hyperthermia.

In order to validate the therapeutic efficacy, we chose the Syrian hamster model to induce oral cancer using DMBA, as DMBA-induced oral tumors in hamsters exhibit biochemical and histopathological features similar to those of human oral cancer. Preliminary in vivo studies using AS-IONPs injected into hamster buccal pouch tumors showed prolonged retention under an alternating magnetic field (AMF) for up to six weeks, while those without AMF were cleared within six days (Fig. 7a and b). Exposure to 100 kHz and 2–12 kA m^{-1} maintained tumor temperature at ∼44 °C for 30 minutes over two sessions, inducing inflammation, necrosis, and subsequent tumor shrinkage by day 11 (Fig. 7c and d). Treated animals exhibited significant tumor reduction or complete regression with improved survival. As hamster tumors were small (<20 mm^3), further efficacy studies were extended to a xenograft nude mouse model for better clinical relevance.[58] Validation of therapeutic efficacy for treating locally advanced tumors requires animal models with larger tumor volumes. Therefore, we employed a patient-derived xenograft (PDX) model using the SCC-25 oral cancer cell line. SCC-25 cells, derived from a tumor originating in the oral cavity due to tobacco consumption, retain the genomic characteristics of human oral cancer in the PDX setting.[59] This model necessitates the use of immunocompromised nude mice to prevent implant rejection. In magnetic hyperthermia therapy (MHT) research, the choice of tumor model—patient-derived xenograft (PDX) or carcinogen-induced—critically impacts translational validity, therapeutic outcomes, and immune assessment. PDX models, created by implanting human tumors/derived cell lines into immunodeficient mice, preserve native heterogeneity, stromal architecture, and genetic integrity, enabling realistic evaluation of nanoparticle heating and intratumoral penetration in clinically relevant settings. These models are ideal for precision oncology studies combining MHT with chemo- or radiotherapy, though their immunodeficiency limits evaluation of immunogenic cell death (ICD) and immune-driven tumor regression.[60–62] In contrast, carcinogen-induced tumor models (e.g., 4NQO-induced oral cancer or DMBA-induced breast cancer) develop tumors within an immunocompetent host, allowing study of MHT's interactions with immune cells, heat-shock response, and vascular remodeling-a physiologically intact context. These

models replicate tumor initiation, progression, and immune evasion, enabling exploration of MHT's role as an ICD inducer and its potential to synergize with checkpoint inhibitors. However, they exhibit higher biological variability and slower tumor formation compared with PDX models.[63–66] Thus, PDX models are optimal for human tumor heat response and precision translation, while carcinogen-induced models are superior for studying immune mechanisms and long-term therapeutic efficacy in MHT research.

As evident from the above discussion, patient-derived xenograft (PDX) models have been widely employed in preclinical cancer research because they closely replicate human tumor biology and therapeutic responses. However, very few studies have explored their application in magnetic hyperthermia-based treatment of oral cancer. Zhao et al.[67] reported a preliminary investigation on magnetic hyperthermia therapy for head and neck squamous cell carcinoma (HNSCC). ~15 nm MNPs were intratumorally injected into Tu212 xenograft-bearing mice and exposed to an alternating magnetic field (AMF, 130 kHz, 7 kA m^{-1}), maintaining tumor temperatures between 40–50 °C for 20 minutes. Histopathological analyses revealed extensive ulceration and coagulative necrosis, with minimal caspase activation, indicating oncotic necrosis as the dominant mechanism. Their findings indicated that hyperthermia-induced cytotoxicity primarily resulted from oncotic necrosis rather than apoptosis, highlighting the distinct cellular mechanisms involved in heat-mediated tumor destruction. These results underscore the need for further detailed studies to elucidate the underlying molecular pathways and optimize treatment parameters for improved therapeutic outcomes in oral cancer.

Similar to the hamster model, early-stage tumors (~100 mm^3) in nude mice also completely regressed after five sessions of magnetic hyperthermia therapy (Fig. 8e). However, since magnetic hyperthermia is clinically relevant for treating locally advanced, unresectable tumors, we evaluated its efficacy in mice bearing larger tumors (>100 mm^3). When therapy was initiated in tumors larger than 100 mm^3, tumor growth was progressively suppressed with increasing treatment sessions (3, 7, and 12 sessions; Fig. 8e). Based on the initial tumor suppression, the number of sessions was extended up to 12 to assess the therapeutic effect of multiple sessions. Overall, while magnetic hyperthermia alone could not completely eradicate large tumors, it effectively slowed tumor progression and may serve as a useful component in combination therapy for better treatment outcomes.

Taboga et al. reported polyphosphate-coated maghemite nanoparticles exhibited dose-dependent cytotoxicity in UM-SCC14A cells (OSCC) with minimal toxicity at intermediate concentrations. In other study related to DMBA-induced oral tumors in Syrian hamsters, MHT was given at 1 MHz and 40 Oe for 15 minutes across three sessions. Treated animals showed significant tumor regression, confirmed histologically, achieving complete remission (12/12 cases) within seven days without systemic toxicity—underscoring the strong therapeutic potential of MHT in oral cancer.[68] Further, a targeted MHT approach employed APTES-coated Fe$_3$O$_4$ nanoparticles conjugated with anti-αvβ6 monoclonal antibody (E7P6) to selectively ablate αvβ6-overexpressing OSCC cells. Upon AMF exposure (174 kHz, 97 Oe), αvβ6-positive VB6 cells showed 85% cell death versus ~20% in αvβ6-negative H357 cells, confirming receptor-specific thermal ablation.[69] In another study related to triple-negative breast cancer (TNBC), ferrimagnetic vortex-domain iron oxide nanorings (FVIOs; 50 nm, M_s = 68 emu g^{-1}) exhibited exceptionally high specific absorption rates (2622 W g^{-1}) under AMF (400 Oe, 360 kHz). In vitro, MHT reduced MDA-MB-231 and 4T1 cell viability to ~10%. In vivo, FVIO-mediated MHT induced immunogenic cell death and a 61% reduction in tumor weight in immunocompetent 4T1-bearing mice, but negligible response in immunodeficient hosts—highlighting an immune-dependent therapeutic mechanism. FVIOs maintained high biocompatibility and biosafety.[70] While these studies establish its efficacy as both a cytotoxic and immunomodulatory cancer therapy, most are conducted at >100 kHz. In contrast, our 100 kHz low-intensity AMF approach represents a clinically pragmatic and physiologically safe hyperthermia window.

Furthermore, the expression of p53 is essential to determine the cancer progenesis and therapeutic response.[71] The follow-up xenograft nude mice study, explored how the expression of the p53 protein changes in tumor tissues under different treatment conditions, using immunohistochemistry as the primary detection method (Fig. 9). The results were consistent with what is commonly understood about p53 in cancer biology, but they also offered some interesting points for reflection. In the reference (normal) tissue samples, p53 expression was either completely absent or very minimal, which aligns with the expected behavior of wild type p53 in healthy cells. These findings served as a valuable baseline, helping us distinguish between normal and abnormal expression patterns in tumor tissues. The most striking observations came from the AMF-only group, where the tumor samples showed intense, wide-spread nuclear staining. This pattern strongly suggests p53 overexpression, which is often linked to mutations in the TP53 gene. Such mutations can cause the protein to accumulate in the nucleus without performing its usual tumor-suppressing functions. This is frequently seen in high-grade tumors and supports the idea that p53 overexpression is not just a marker but a reflection of underlying genetic instability.[49] On the other hand, tumor tissues that had been treated showed much milder p53 staining, ranging from focal to mild intensity (Fig. 8). While this doesn't confirm that the treatments corrected the TP53 mutation, the reduced expression may indicate a shift in tumor behavior, potentially pointing to less aggressive cell activity or a partial restoration of regulatory pathways. It raises the possibility that treatment may have influenced how the tumor cells handle stress or respond to DNA damage, even if it is done indirectly. The presence of fibroblasts in some slides offered an internal point of reference. These normal connective tissue cells showed no significant p53 staining, which helped confirm that the overexpression seen in tumor cells was not an artifact or background noise, but a real, localized signal. Another important takeaway is the consistency between the staining patterns observed here and the well-established categories of p53 expression: normal, complete absence, overexpression, and cytoplasmic localization. Although the cytoplasmic pattern

wasn't observed in this study, the other three were clearly identifiable, adding further confidence to the methodology and findings. Altogether, the results reaffirm the value of p53 IHC as both a diagnostic and research tool. It can give us a meaningful glimpse into the molecular landscape of a tumor, and in preclinical settings like this, it may even help evaluate the impact of experimental treatments. While more detailed molecular studies would be needed to draw firm conclusions about TP53 mutation correction, the patterns observed here suggest that treatment-induced changes in p53 expression are worth investigating further. Overall, these results highlight the value of p53 immunohistochemistry as both a diagnostic marker and a tool for evaluating treatment effects on tumor biology. They also emphasize the need to interpret p53 expression within the specific biological and genetic context of each tumor type, given the variability in staining patterns across cancers. Importantly, the intensity and pattern of p53 staining are not universal and can vary across different cancer types, underscoring the need for context-specific interpretation.

Magnetic hyperthermia therapy (MHT), though effective as a standalone modality, significantly enhances standard cancer treatments by increasing cellular heat sensitivity, improving chemotherapeutic uptake, and modulating immune responses. Due to this, its clinical translation possibilities are being explored actively, and it has been found to enhance the treatment outcomes particularly in recurrent, previously irradiated, or poorly immunogenic tumors. For instance, a recent phase II clinical trial combined MHT with concurrent chemoradiotherapy (CCRT) in 35 patients with non-metastatic, recurrent head and neck cancer unfit for salvage surgery. Patients received 50 Gy in 22 fractions with weekly hyperthermia (42 ± 0.5 °C, 40 min) and cisplatin/docetaxel. The overall response rate reached 82.9%, with a median overall survival of 32.8 months and manageable toxicities, underscoring MHT's clinical benefit.[72] Similarly, nanoparticle-based thermoradiotherapy in 66 patients with recurrent glioblastoma using intratumoral magnetite nanoparticles and stereotactic radiotherapy (30 Gy total) achieved a median survival of 13.4 months from recurrence, demonstrating improved safety and efficacy over standard regimens.[73] In immunotherapy, MHT synergized with checkpoint blockade in a poorly immunogenic B16–F10 melanoma model. Hyperthermia-induced HMGB1 release activated inflammatory pathways, while combined treatment with CpG (TLR9 agonist) and anti-PD-1/CTLA-4 antibodies yielded complete tumor regression in 80% of mice, converting "cold" tumors into immunogenic "hot" tumors.[74] Overall, these findings suggest that integrating MHT with chemo-, radio-, or immunotherapy can reduce drug doses, enhance efficacy, minimize toxicity, and improve patient outcomes in resistant or recurrent cancers.

Experimental

Materials

Ferrous(II) chloride tetrahydrate, ferrous(III) chloride hexahydrate, ammonia solution, (3-aminopropyl) triethoxysilane, acetic acid glacial, hydrochloric acid, hydrocortisone and 7,12-dimethylbenz[a]anthracene (DMBA) were procured from Merk. Dulbecco's Modified Eagle's Medium (DMEM) with Ham's F12 medium, antibiotic 100× and Trypsin were purchased from Thermo Fisher. Fetal bovine serum (FBS) was obtained from MP Biomedicals.

Methods

Stable suspension of iron oxide nanoparticles-preparation and characterization. A stable suspension of polymer coated iron oxide nanoparticles (AS-IONPs) (ThermoHeals™ solution) was synthesized using the chemical co-precipitation technique in nitrogen atmosphere to minimize oxidation and maintain reaction consistency.[75] A three-necked round-bottom flask (RBF) was used for the synthesis, positioned on a heating mantle to achieve uniform thermal distribution. Ferric chloride hexahydrate ($FeCl_3 \cdot 6H_2O$) and ferrous chloride tetrahydrate ($FeCl_2 \cdot 4H_2O$) were separately dissolved in DI water until a clear solution was obtained and subsequently mixed into the flask at approximately 70 °C. Subsequently, 25% aqueous ammonia was introduced dropwise using a glass dropper to avoid abrupt pH changes. A visible color transition from orange to black signaled the formation of iron oxide nanoparticles. The reaction mixture was kept at the same temperature under continuous stirring for an additional period to support particle growth and stabilization. The synthesized nanoparticle suspension was washed repeatedly with DI water by magnetic decantation to eliminate excess ammonia and unreacted salts followed by sonication for one hour to promote particle dispersion and reduce agglomeration. The pH of the suspension was carefully adjusted to a slightly acidic range using diluted hydrochloric acid (prepared in a 4 : 1 DI water to concentrated acid ratio) under continuous stirring. The full duration of sonication was optimized to ensure a uniform and stable nanoparticle suspension. For functionalization, a measured amount of amino silane was added slowly with continuous sonication. About ten minutes post addition, the pH was carefully adjusted to near-neutral conditions by dropwise addition of glacial acetic acid. Nitrogen purging was stopped once sonication was complete. Subsequent dialysis was carried out to remove low-molecular-weight impurities, residual salts, and any unreacted chemicals. Dialysis continued until the conductivity of the external medium decreased to a defined threshold, confirming effective purification. Parameters such as pH, volume before and after dialysis, and conductivity were carefully tracked. After purification, the solution was resuspended in DI water and the required concentration was achieved through controlled evaporation.[76]

Temperature measurement and SAR calculations. Temperature measurements were performed with a medical grade 0.55 mm fibre optic thermometer (TS5, Optocon-Weideman, Germany). For efficacy studies, the sensor was placed directly into the animal tissue using a canula (gauge 22) and temperature readings were taken at 2.5 seconds interval. A closed feedback loop system was used to adjust the incremental power of the AMF generator to achieve and maintain the desired temperature. For SAR measurements, a thermally insulated 1 mL PP tube with cotton, containing 50 μL of 100 mg mL^{-1}

nanoparticle solution was used. The sensor was inserted in the tube and placed in the centre of AMF coil. FOTEMP Plus-OEM signal conditioner was used to measure temperature. The SAR was calculated using the formula:

$$\text{SAR} = \frac{C_{\text{total}}}{m_{\text{NP}}} \left(\frac{\mathrm{d}T}{\mathrm{d}t} \right)$$

where, C_{total} is the total heat capacity of the solvent + IONPs. Considering IONPs contribution negligible, a value of 4.18 J g^{-1}. K for water was taken. m_{NP} is the mass of Fe_3O_4 present calculated based on concentration and volume of solution used. $\mathrm{d}T/\mathrm{d}t$ is the initial slope (K s^{-1}), obtained from linear fit of the initial straight portion of temperature curve.

Zeta-PALS Analyzer (Brookhaven) was employed to determine electrophoretic mobility, zeta potential, and particle size distribution using Phase Analysis Light Scattering (PALS). As our nanoparticle suspension is already prepared and stored in deionized water at a physiologically relevant pH (~7.4), no other modifications in the suspension was done other than dilution for the Dynamic Light Scattering (DLS) measurements. The required diluted sample was prepared by adding 3.5 μL of the sample with 3500 μL of deionized water. The suspension was sonicated for around 3 minutes to disperse aggregates and ensure a uniform suspension before being analyzed in the DLS machine five times, with each measurement lasting 15 seconds at 25 °C in water (RI = 1.330, viscosity = 0.890 cP) using a 658 nm laser at 90°. The intensity-weighted distribution was corrected for Mie scattering using particle refractive index (RI = 1.500) to obtain number- and volume-weighted size distributions. Zeta potential analysis was conducted to determine the surface charge of the particles. The samples were not filtered before the measurement.

Crystal structure determination and phase purity studies were carried out using an X-ray diffractor (Rigaku Smart lab) with a copper anode and utilizing Cu Kα (λ = 1.5404 Å) radiation. Magnetic property measurement data for the synthesized nanoparticles was obtained by using a vibrating sample magnetometer (VSM-Lake Shore instrument, Westerville, OH, USA). Fourier Transform Infrared Spectroscopy (FTIR) (PerkinElmer-Frontier) provides valuable information about the chemical composition and structure of a sample. The samples were desiccated under vacuum for 72 hours to ensure complete removal of residual water. A dry sample was mixed with potassium bromide (KBr), compressed into a uniform pellet using a hydraulic press, and placed in the FTIR instrument for spectral characterization. The recorded infrared absorbance data was processed using Origin software, and a graph was plotted to interpret absorption peaks with corrected baseline. Iron content in the ThermoHeals solution was estimated using inductively coupled plasma mass spectrometry (ICPMS-Thermo fisher scientific, iCPRQ).

Transmission Electron Microscopy (TEM) (Thermo Fisher Scientific, Titan 300 Themis D 3391) was utilized for detailed structural and elemental analysis. The sample preparation involved diluting it with deionized water until only a trace of color remained, ensuring optimal transparency for imaging. The diluted sample was then subjected to 30 minutes of sonication to achieve proper dispersion of nanoparticles. A small drop of the sonicated sample was carefully placed onto a carbon coated grid with mesh size 300 using precision tweezers. The grid was positioned on filter paper and dried under red light for 8 hours followed by 24 hours of desiccation to eliminate any residual moisture, ensuring complete dryness before analysis. TEM analysis included Selected Area Diffraction Pattern (SADP) to examine crystallinity and elemental mapping for Fe, Si, C, O, N, and H, facilitating a comprehensive understanding of sample composition. ImageJ software was used to measure and determine the nanoparticle size distribution accurately, facilitating the precise characterization of particle size and distribution trends. The alternating magnetic field (AMF) generator was constructed in-house, producing a frequency of 100 kHz and a magnetic field intensity ranging from 0 to 12 kA m^{-1}. It consists of a 30 cm diameter solenoid coil made of hollow copper tubes. DI water runs through the hollow tube in a closed circuit to dissipate the heat generated from eddy currents at 100 kHz.

***In vitro* and *in vivo* compatibility studies.** The SCC-25 (ATCC) cell line was used for the study. These cells were cultured in a complete growth medium composed of a 1:1 mixture of Dulbecco's Modified Eagle's Medium (DMEM) and Ham's F12 medium, containing 1.2 g per L sodium bicarbonate, 2.5 mM L-glutamine, 15 mM HEPES, and 0.5 mM sodium pyruvate. Additionally, the medium was supplemented with 400 ng per mL hydrocortisone and 10% fetal bovine serum (FBS) to support optimal cell growth and maintenance. The cytotoxicity of the synthesized IONPs was determined by using an MTT assay. The 96 well plate was seeded with 10K cells. Before adding the samples to the cells, the suspension was sterilized by autoclaving at 121 °C and 15 psi for 20 minutes. The different concentration of nanoparticles was used for the study by diluting the nanoparticles' concentration (150 mg mL^{-1}) with the media. The working serial diluted concentrations were 0.5 mg mL^{-1}, 1 mg mL^{-1}, 2 mg mL^{-1}, 4 mg mL^{-1}, 6 mg mL^{-1}, 8 mg mL^{-1}, 10 mg mL^{-1}, 15 mg mL^{-1}. After 4–6 h of seeding the plate, the suspension of nanoparticles was added as per the concentration. The plate was incubated for different time intervals 24 h, 48 h, 72 h from the seeding time, then 200 μL MTT solution (0.5 mg mL^{-1}) was added. The plate was incubated for 4 h at 37 °C, MTT reagent was removed followed by the addition of 200 μL of DMSO. The solution of each concentration was taken for centrifugation at 5000 rpm for 2 minutes (to remove the nanoparticles content which may interfere with the formazan concentration). The absorbance was recorded at 590 nm in the Skanlt software.

Cell staining experiments were carried out on 24 well plates with cover slips, which were seeded with 50k cells per mL of SCC-25 cells. Different concentrations of amino silane coated nanoparticles were prepared by diluting the nanoparticles' concentration (150 mg mL^{-1}) with the media. The working serially diluted concentrations were 0.5 mg mL^{-1}, 1 mg mL^{-1}, 2 mg mL^{-1}, 4 mg mL^{-1}, 6 mg mL^{-1}, 8 mg mL^{-1}, 10 mg mL^{-1}, 15 mg mL^{-1}. After 4–6 h of seeding the plate, the suspension of nanoparticles was added as per the concentration. The plates were incubated for different time intervals of 24 h, 48 h, and

72 h from the seeding time, followed by the staining procedure after the completion of each time scale. The suspension was removed, and the cells were gently rinsed with 1× PBS. The cells were fixed with 3.7% formaldehyde in 1× PBS for 20 minutes. Subsequently, each step was followed by washing with 1× PBS. Next, the cells were permeabilized with 0.1% Triton X-100 in PBS for 10 minutes. The cells were blocked by 1% BSA in 1× PBS for 20 minutes. Cell staining was performed by ActinGreen 488 ReadyProbes Reagent (AlexaFluor 488 phalloidin), followed by 30 minutes of incubation at room temperature in the dark. Nuclear staining was performed by Hoechst 33342 (Invitrogen H1399) dye and incubated for 5–10 minutes. This was followed by washing the cells twice with 1 PBS prior to observation under fluorescence microscope (Olympus, Cellsense software).

Biodistribution and clearance studies using a rat model. All animal experiments were conducted at Radiant Research Services Pvt Ltd, Bangalore, India, in accordance with the guidelines of the Committee for the Control and Supervision of Experiments on Animals. The study protocol was approved by the Institutional Animal Ethical Committee (IAEC) of Radiant Research Services Pvt Ltd. The study was performed as per ISO 10993-11:2017, Biological Evaluation of Medical Devices – Part 11: Tests for systemic toxicity. Female Albino Wistar rats (8–10 weeks old) were randomly divided into three groups: G1 (control, saline only), G2 (low-dose group, IONPs solution 150 mg mL^{-1}), and G3 (high-dose group, AS-IONPs solution 300 mg mL^{-1}). Throughout the experiment, all animals were provided with a chow diet (Purina lab diet 5L79 Rat and Mouse 18%) and fresh, uncontaminated drinking water.[77] Animals were observed for abnormal behavior and signs of biological reactivity at time intervals of 4, 24, 48 and 72 h post administration. Approximately 0.5 mL of blood was collected from each rat at specific time points—0 h (pre-dose), and at 0.5-, 4-, 6-, 24-, 48-, and 72-hours post-dose—in EDTA-containing tubes. Serum iron levels were quantified using the ICPMS method to determine the reference standard in rat plasma. Hematological and biochemical profiles were analyzed after 72 hours of injection. H&E staining was used to study histopathological changes in the heart, spleen, liver, kidneys and lungs and to rule out any accumulation of IONPs.

***In vivo* magnetic hyperthermia efficacy study.** All animal experiments were conducted at Radiant Research Services Pvt Ltd, Bangalore, India, in accordance with the guidelines of the Committee for the Control and Supervision of Experiments on Animals (CCSEA). The study protocol was approved by the Institutional Animal Ethical Committee (IAEC) of Radiant Research Services Pvt Ltd (IAEC Number: RR/IAEC/126-2024).

The feasibility and efficacy of the treatment were evaluated using male Syrian hamsters aged 8 to 10 weeks, as DMBA-induced oral squamous cell carcinoma (SCC) in hamsters closely mimics the biochemical and histopathological features of human oral cancer. Tumors were induced in the buccal cavity of the hamsters by applying a 0.5% solution of 7,12-dimethylbenzanthracene (DMBA) in liquid paraffin to the right buccal pouches three times per week. Treatment was initiated once the tumor volume exceeded 15 mm^3.

As tumor induction in hamsters is a slow process and the maximum tumor size is only a few millimeters, we also conducted efficacy studies using a xenograft nude mice model. Athymic Nude Mice Foxn1, aged 6 to 7 weeks, were selected for the study. Throughout the experiment, the nude mice were maintained in individually ventilated cages (IVCs) and provided with a Purina Lab Diet 5L79 (18% protein Rat and Mouse Diet) and fresh, uncontaminated drinking water. Each mouse was subcutaneously injected in the lower flank with 200 μL of a suspension containing 10^6 SCC-25 cancer cells, ensuring consistent tumor development. Following the injection, the mice were allowed a period of 1–3 weeks for tumor growth, with tumors expected to reach a targeted volume of above 100 mm^3.

Tumor volume. Tumor size was measured using digital calipers, and the volume (in mm^3) was calculated using the following standard formula:

$$\text{Tumor volume} = \frac{\text{length} \times \text{width}^2}{2}$$

Treatment. When the tumor size reached above 100 mm^3 in the PDX model and above 20 mm^3 in the hamster model, nanoparticles at a concentration of 150 mg mL^{-1} (50 μL cm^{-3}) were injected directly into the tumor. The body weight of the mice and the tumor size were measured prior to each hyperthermia session. Anesthesia was administered to the animals, which were then placed inside the alternating magnetic field (AMF) coil. The AMF frequency of 100 kHz and magnetic intensity were automatically adjusted to maintain the temperature at the tumor site between 43–46 °C throughout the session. Temperature changes were continuously monitored using a fiber optic thermometer (Weidmann Technologies Deutschland, GmbH).

After each thermal session, tumor size was measured and recorded to track any changes in response to the treatment. Tumor growth or regression was systematically analyzed over multiple sessions, allowing for a comprehensive evaluation of the efficacy of the hyperthermia treatment in controlling tumor progression. This structured approach ensured accurate and consistent tumor size assessments, providing a reliable evaluation of the treatment's effectiveness.

CT scans. To evaluate the accumulation of nanoparticles at the target site, a non-destructive imaging approach using computed tomography (CT) was employed. The scans were acquired using a clinical CT scanner (GE Revolution ACT, 32-slice). However, due to restricted system access and the absence of calibrated quantitative data in the exported images, reliable region of interest (ROI) intensity measurements could not be performed. Therefore, the analysis was limited to a qualitative assessment of the CT images.

Following anesthesia administration, the animals were subjected to CT scanning to obtain cross-sectional images of the relevant anatomical regions. As exposure to an alternating magnetic field (AMF) can potentially induce nanoparticle agglomeration, thereby delaying their clearance from the implantation site, CT imaging was performed to monitor this effect. Accordingly, CT scans were conducted at intervals of 3 to

6 weeks, both in AMF-exposed and non-exposed groups, after intratumoral injection of AS-IONPs. The scans were acquired using the parameters 140 kV and 80 mA. After 5 min of procedure, the animal was taken out of the machine.

Immunohistochemistry of p53. The tumor tissue treated and untreated were analysed for p53 expression using immunohistochemistry. Formalin-fixed, paraffin-embedded tissue sections (4 μm thick) were deparaffinized in xylene and rehydrated through graded alcohols. Antigen retrieval was performed by heating the sections in citrate buffer (pH 6.0) at 95 °C for 20 minutes. Endogenous peroxidase activity was blocked using 3% hydrogen peroxide in methanol for 10 minutes at room temperature. After washing in phosphate-buffered saline (PBS), sections were incubated with a mouse monoclonal anti-p53 antibody for 1 hour at room temperature. Following primary antibody incubation, sections were washed and incubated with a biotinylated secondary antibody for 30 minutes, followed by streptavidin–horseradish peroxidase for another 30 minutes. Color was developed using 3,3′-diaminobenzidine (DAB) chromogen, and counterstaining was performed with Mayer's hematoxylin. Slides were dehydrated, cleared, and mounted with DPX mounting medium. The H-score for p53 immunohistochemistry was calculated using ImageJ by quantifying the intensity and percentage of positively stained nuclei. Images were deconvoluted to isolate DAB staining, and intensity thresholds were set to categorize cells as 1+ (weak), 2+ (moderate), or 3+ (strong).

Statistical analysis

The MTT assay results are presented as the mean $\pm$ standard deviation (SD) from five independent experiments ($N = 5$), each performed in triplicate ($n = 3$). Statistical significance was evaluated using two-way ANOVA followed by Sidak's multiple comparisons *post hoc* test.

For the animal tumor regression studies, data are expressed as the mean $\pm$ standard error of the mean (SEM). A two-way ANOVA (or mixed-effects analysis, where appropriate) followed by Tukey's multiple comparisons test was used to assess differences among treatment groups over time. To illustrate biological variability, individual animal data points have been overlaid on the plots.

A p-value ≤ 0.05 was considered statistically significant. All statistical analyses were performed using GraphPad Prism (GraphPad Software, San Diego, CA, USA).

Conclusions

This study demonstrated that amino silane-coated iron oxide nanoparticles are safe and effective for magnetic hyperthermia treatment of oral squamous cell carcinoma. *In vivo* studies highlight the importance of repeated sessions for sustained tumor suppression. Tumors ≤ 100 mm^3 responded well, often showing reversal, while larger tumors (>100 mm^3) showed partial eradication and slowed growth. Changes in p53 expression as a function of repeated MHT sessions indicate improved prognosis and a potential reduction in recurrence risk. These observations indicate that MH therapy exerts dual effects: direct physical destruction of tumor tissue and molecular modulation of oncogenic pathways. By progressively lowering mutant p53 expression, MH treatment appears to target resistant tumor subpopulations, reduce intratumoral heterogeneity, and induce apoptosis in aggressive clones. Overall, both histological and tumor volume data confirm that repeated MH exposures produce significant therapeutic benefit, not only through hyperthermic tumor eradication but also by normalizing molecular signatures associated with cancer progression. This highlights MH therapy as a promising approach capable of integrating physical and molecular mechanisms to achieve durable tumor control and potential remission in solid cancers. Further, these findings suggest that while magnetic hyperthermia alone holds significant promise, it may require combination with other modalities such as radiation therapy or chemotherapy to achieve complete eradication of larger tumor volumes. Future studies should therefore explore synergistic effects with conventional treatment regimens to further optimize therapeutic outcomes and extend the applicability of this approach to more challenging clinical scenarios.

Conflicts of interest

There are no conflicts to declare.

Data availability

The data supporting this article have been included as part of the supplementary information (SI). Supplementary information is available. See DOI: https://doi.org/10.1039/d5ra06567d.

Acknowledgements

References

1 P. H. Montero and S. G. Patel, Cancer of the Oral Cavity, *Surg. Oncol. Clin.*, 2015, **24**, 491–508.

2 R. Sun, W. Dou, W. Liu, J. Li, X. Han, S. Li, *et al.*, Global, regional, and national burden of oral cancer and its attributable risk factors from 1990 to 2019, *Cancer Med.*, 2023, **12**(12), 13811–13820.

3 F. Bray, J. Ferlay, I. Soerjomataram, R. L. Siegel, L. A. Torre and A. Jemal, Global cancer statistics 2018: GLOBOCAN estimates of incidence and mortality worldwide for 36 cancers in 185 countries, *Ca-Cancer J. Clin.*, 2018, **68**(6), 394–424.

4   L. Xie and Z. Shang, Burden of oral cancer in Asia from 1990 to 2019: Estimates from the Global Burden of Disease 2019 study, *PLoS One*, 2022, **17**(3), e0265950.

5   F. Bray, J. Ferlay, I. Soerjomataram, R. L. Siegel, L. A. Torre and A. Jemal, Global cancer statistics 2018: GLOBOCAN estimates of incidence and mortality worldwide for 36 cancers in 185 countries, *Ca-Cancer J. Clin.*, 2018, **68**(6), 394–424.

6   D. Pulte and H. Brenner, Changes in Survival in Head and Neck Cancers in the Late 20th and Early 21st Century: A Period Analysis, *Oncologist*, 2010, **15**(9), 994–1001.

7   D. Hanahan and R. A. Weinberg, The Hallmarks of Cancer Review evolve progressively from normalcy via a series of pre, *Cell*, 2000, **100**(1), 57–70.

8   M. Hurwitz and P. R. Stauffer, Hyperthermia, radiation and chemotherapy: the role of heat in multidisciplinary cancer care, *Semin. Oncol.*, 2014, **41**(6), 714–729.

9   C. F. Babbs and D. P. Dewitt, Physical principles of local heat therapy for cancer, *Med. Instrum.*, 1981, **15**(6), 367–373.

10 J. Wang, L. Wan, G. Huang, C. Chen and Y. Wu, Comparison of high-intensity focused ultrasound and microwave ablation for the treatment of small liver metastatic tumors, *J. Int. Med. Res.*, 2023, **51**(4), 1–12.

11 High Intensity Focused Ultrasound (HIFU), Available from: http://www.wecarecancer.com/hifu-high-intensity-focused-ultrasound/.

12 H. P. Kok, E. N. K. Cressman, W. Ceelen, C. L. Brace, R. Ivkov, H. Grüll, *et al.*, Heating technology for malignant tumors: a review, *Int. J. Hyperthermia*, 2020, **37**, 711–741.

13 Y. Zhang and Y. Zhai, Magnetic Induction Heating of Nano-sized Ferrite Particles, *Advances in Induction and Microwave Heating of Mineral and Organic Materials*, 2011, iss. 1.

14 N. Levine and J. G. Rothschild, Treatment of Mycobacterium chelonae infection with controlled localized heating, *J. Am. Acad. Dermatol.*, 1991, **24**(5), 867–870.

15 M. E. Sadat, R. Patel, S. L. Bud'Ko, R. C. Ewing, J. Zhang, H. Xu, *et al.*, Dipole-interaction mediated hyperthermia heating mechanism of nanostructured Fe3O4 composites, *Mater. Lett.*, 2014, **129**, 57–60, DOI: 10.1016/j.matlet.2014.05.001.

16 A. Jordan, P. Wust, H. Fähling, W. John, A. Hinz and R. Felix, Inductive heating of ferrimagnetic particles and magnetic fluids: Physical evaluation of their potential for hyperthermia, *Int. J. Hyperthermia*, 2009, **25**(7), 499–511.

17 V. Narayanaswamy, I. M. Obaidat, S. Latiyan, S. Jain, C. Nayek, S. Goankar, *et al.*, Role of interface quality in iron oxide core/shell nanoparticles on heating efficiency and transverse relaxivity, *Mater. Express*, 2019, **9**(4), 328–336.

18 A. Jordan, P. Wust, H. Fähling, W. John, A. Hinz and R. Felix, Inductive heating of ferrimagnetic particles and magnetic fluids: Physical evaluation of their potential for hyperthermia, *Int. J. Hyperthermia*, 2009, **25**(7), 499–511.

19 P. Pradhan, J. Giri, G. Samanta, H. D. Sarma, K. P. Mishra, J. Bellare, *et al.*, Comparative evaluation of heating ability and biocompatibility of different ferite-based magnetic fluids for hyperthermia application, *J. Biomed. Mater. Res., Part B*, 2007, **81**(1), 12–22.

20 I. M. Obaidat, B. Issa and Y. Haik, Magnetic properties of magnetic nanoparticles for efficient hyperthermia, *Nanomaterials*, 2014, **5**, 63–89.

21 M. Bañobre-López, A. Teijeiro and J. Rivas, Magnetic nanoparticle-based hyperthermia for cancer treatment, *Rep. Practical Oncol. Radiother.*, 2013, **18**, 397–400.

22 R. A. Bohara and S. Leporatti, Translational Hurdles with Magnetic Nanoparticles and Current Clinical Scenario in Hyperthermia Applications, *Magnetochemistry*, 2022, **8**(10), 123.

23 S. Behzadi, V. Serpooshan, W. Tao, M. A. Hamaly, M. Y. Alkawareek, E. C. Dreaden, *et al.*, Cellular uptake of nanoparticles: Journey inside the cell, *Chem. Soc. Rev.*, 2017, **46**, 4218–4244.

24 N. D. Donahue, H. Acar and S. Wilhelm, Concepts of nanoparticle cellular uptake, intracellular trafficking, and kinetics in nanomedicine, *Adv. Drug Delivery Rev.*, 2019, **143**, 68–96.

25 B. Rothen-Rutishauser, J. Bourquin and A. Petri-Fink, Nanoparticle-cell interactions: Overview of uptake, intracellular fate and induction of cell responses, *Nanosci. Technol.*, 2019, 153–170, DOI: 10.1007/978-3-030-12461-8_6.

26 Q. Feng, Y. Liu, J. Huang, K. Chen, J. Huang and K. Xiao, Uptake, distribution, clearance, and toxicity of iron oxide nanoparticles with different sizes and coatings, *Sci. Rep.*, 2018, **8**(1), 2082.

27 S. Salatin and A. Yari Khosroushahi, Overviews on the cellular uptake mechanism of polysaccharide colloidal nanoparticles, *J. Cell. Mol. Med.*, 2017, **21**, 1668–1686.

28 J. Mosquera, I. García and L. M. Liz-Marzán, Cellular Uptake of Nanoparticles versus Small Molecules: A Matter of Size, *Acc. Chem. Res.*, 2018, **51**(9), 2305–2313.

29 D. A. Kuhn, D. Vanhecke, B. Michen, F. Blank, P. Gehr, A. Petri-Fink, *et al.*, Different endocytotic uptake mechanisms for nanoparticles in epithelial cells and macrophages, *Beilstein J. Nanotechnol.*, 2014, **5**(1), 1625–1636.

30 H. J. Shin, M. Kwak, S. Joo and J. Y. Lee, Quantifying fluorescent nanoparticle uptake in mammalian cells using a plate reader, *Sci. Rep.*, 2022, **12**(1), 20146.

31 C. He, Y. Hu, L. Yin, C. Tang and C. Yin, Effects of particle size and surface charge on cellular uptake and biodistribution of polymeric nanoparticles, *Biomaterials*, 2010, **31**(13), 3657–3666.

32 F. Toscano and M. Torres-Arias, Nanoparticles cellular uptake, trafficking, activation, toxicity and in vitro evaluation, *Curr. Res. Immunol.*, 2023, **4**, 100073.

33 W. J. Atkinson, I. A. Brezovich and D. P. Chakraborty, Usable Frequencies in Hyperthermia with Thermal Seeds, *IEEE Trans. Biomed. Eng.*, 1984, 70–75.

34 K. Maier-Hauff, F. Ulrich, D. Nestler, H. Niehoff, P. Wust, B. Thiesen, *et al.*, Efficacy and safety of intratumoral thermotherapy using magnetic iron-oxide nanoparticles combined with external beam radiotherapy on patients with recurrent glioblastoma multiforme, *J. Neuro-Oncol.*, 2011, **103**(2), 317–324.

35 K. Maier-Hauff, R. Rothe, R. Scholz, U. Gneveckow, P. Wust, B. Thiesen, et al., Intracranial thermotherapy using magnetic nanoparticles combined with external beam radiotherapy: Results of a feasibility study on patients with glioblastoma multiforme, J. Neuro-Oncol., 2007, 81(1), 53–60.

36 F. Rodríguez, P. Caruana, N. De la Fuente, P. Español, M. Gámez, J. Balart, et al., Nano-Based Approved Pharmaceuticals for Cancer Treatment: Present and Future Challenges, Biomolecules, 2022, 12, 784.

37 A. A. Roslan, S. N. A. Zaine, H. Mohd Zaid, M. Umar and H. G. Beh, Nanofluids stability on amino-silane and polymers coating titanium dioxide and zinc oxide nanoparticles, Eng. Sci. Technol., 2023, 37, 101318.

38 M. H. Mashhadizadeh and M. Amoli-Diva, Drug-carrying amino silane coated magnetic nanoparticles as potential vehicles for delivery of antibiotics, J. Nanomed. Nanotechnol., 2012, 3(4), 1000139.

39 I. A. F. Urquizo, T. C. H. García, S. L. Loredo, J. T. E. Galindo, P. E. G. Casillas, J. C. S. Barrón, et al., Effect of Aminosilane Nanoparticle Coating on Structural and Magnetic Properties and Cell Viability in Human Cancer Cell Lines, Part. Part. Syst. Charact., 2022, 39(10), 2200106.

40 E. G. Karvelas, N. K. Lampropoulos, L. T. Benos, T. Karakasidis and I. E. Sarris, On the magnetic aggregation of Fe3O4 nanoparticles, Comput. Methods Programs Biomed., 2021, 198, 105778.

41 H. Zheng, J. Schenk, D. Spreitzer, T. Wolfinger and O. Daghagheleh, Review on the Oxidation Behaviors and Kinetics of Magnetite in Particle Scale, Steel Res. Int., 2021, 92, 2000687.

42 I. Berktas, A. N. Ghafar, P. Fontana, A. Caputcu, Y. Menceloglu and B. S. Okan, Facile synthesis of graphene from waste tire/silica hybrid additives and optimization study for the fabrication of thermally enhanced cement grouts, Molecules, 2020, 25(4), 886.

43 H. Namduri and S. Nasrazadani, Quantitative analysis of iron oxides using Fourier transform infrared spectrophotometry, Corros. Sci., 2008, 50(9), 2493–2497.

44 G. Zambzickaite, M. Talaikis, J. Dobilas, V. Stankevic, A. Drabavicius, G. Niaura, et al., Microwave-Assisted Solvothermal Synthesis of Nanocrystallite-Derived Magnetite Spheres, Materials, 2022, 15(11), 4008.

45 IR Spectroscopy Tutorial: Amines.

46 L. Nalbandian, E. Patrikiadou, V. Zaspalis, A. Patrikidou, E. Hatzidaki and C. N. Papandreou, Magnetic Nanoparticles in Medical Diagnostic Applications: Synthesis, Characterization and Proteins Conjugation, Curr. Nanosci., 2015, 12(4), 455–468.

47 A. Schedle, P. Samorapoompichit, X. H. Rausch-Fan, A. Franz, W. Füreder, W. R. Sperr, et al., Response of L-929 Fibroblasts, Human Gingival Fibroblasts, and Human Tissue Mast Cells to Various Metal Cations, J. Dent. Res., 1995, 74(8), 1513–1520.

48 A. V. Singh, Y. Alapan, T. Jahnke, P. Laux, A. Luch, A. Aghakhani, et al., Seed-mediated synthesis of plasmonic gold nanoribbons using cancer cells for hyperthermia applications, J. Mater. Chem. B, 2018, 6(46), 7573–7581.

49 K. W. Thiel, E. J. Devor, V. L. Filiaci, D. Mutch, K. Moxley, A. Alvarez Secord, et al., TP53 Sequencing and p53 Immunohistochemistry Predict Outcomes When Bevacizumab Is Added to Frontline Chemotherapy in Endometrial Cancer: An NRG Oncology/Gynecologic Oncology Group Study, J. Clin. Oncol., 2022, 40, 3289–3300.

50 B. Murnyák and T. Hortobágyi, Immunohistochemical correlates of TP53 somatic mutations in cancer, Oncotarget, 2026, 7, 64910–64920.

51 A. V. Singh, T. Jahnke, S. Wang, Y. Xiao, Y. Alapan, S. Kharratian, et al., Anisotropic Gold Nanostructures: Optimization via in Silico Modeling for Hyperthermia, ACS Appl. Nano Mater., 2018, 1(11), 6205–6216.

52 D. B. Sabzi, A. Jafari, M. Vafaie-Sefti, R. Saber and Z. Fakhroueian, Preparation of stable colloidal dispersion of surface modified Fe3O4 nanoparticles for magnetic heating applications, Sci. Rep., 2024, 14(1), 1296.

53 O. Karaagac and H. Köçkar, Improvement of the saturation magnetization of PEG coated superparamagnetic iron oxide nanoparticles, J. Magn. Magn. Mater., 2022, 551, 169140.

54 A. Nasser, A. Qdemat, H. Unterweger, R. Tietze, X. Sun, J. Landers, et al., Impact of coating type on structure and magnetic properties of biocompatible iron oxide nanoparticles: insights into cluster organization and oxidation stability, Phys. Chem. Chem. Phys., 2024, 26(38), 24912–24923.

55 X. Liu, Y. Zhang, Y. Wang, W. Zhu, G. Li, X. Ma, et al., Comprehensive understanding of magnetic hyperthermia for improving antitumor therapeutic efficacy, Theranostics, 2020, 10(8), 3793–3815.

56 P. Tiwari, S. Agarwal, S. Srivastava and S. Jain, The combined effect of thermal and chemotherapy on HeLa cells using magnetically actuated smart textured fibrous system, J. Biomed. Mater. Res., Part B, 2018, 106(1), 40–51.

57 N. Waldoefner and A. Jordan, Agglomerating magnetic alkoxysilane-coated nanoparticles, US Pat., 9962442, 2016.

58 D. A. B. Martínez, P. A. Barato Gómez, C. A. Iregui Castro and J. E. Rosas Pérez, DMBA-Induced Oral Carcinoma in Syrian Hamster: Increased Carcinogenic Effect by Dexamethasone Coexposition, BioMed Res. Int., 2020, 2020, 1470868.

59 Y. Liu, W. Wu, C. Cai, H. Zhang, H. Shen and Y. Han, Patient-derived xenograft models in cancer therapy: technologies and applications, Signal Transduction Targeted Ther., 2023, 8, 160.

60 H. Gao, J. M. Korn, S. Ferretti, J. E. Monahan, Y. Wang, M. Singh, et al., High-throughput screening using patient-derived tumor xenografts to predict clinical trial drug response, Nat. Med., 2015, 21(11), 1318–1325.

61 M. Hidalgo, F. Amant, A. V. Biankin, E. Budinská, A. T. Byrne, C. Caldas, et al., Patient-derived Xenograft models: An emerging platform for translational cancer research, Cancer Discovery, 2014, 4(9), 998–1013.

62 V. Janitri, K. N. ArulJothi, V. M. Ravi Mythili, S. K. Singh, P. Prasher, G. Gupta, et al., The roles of patient-derived xenograft models and artificial intelligence toward precision medicine, MedComm, 2024, 5, e745.

63 Y. Liu, T. Yin, Y. Feng, M. M. Cona, G. Huang, J. Liu, *et al.*, Mammalian models of chemically induced primary malignancies exploitable for imaging-based preclinical theragnostic research, *Quant. Imag. Med. Surg.*, 2015, **5**(5), 708–729. http://www.ncbi.nlm.nih.gov/pubmed/26682141.

64 D. Krewski, J. M. Rice, M. Bird, B. Milton, B. Collins, P. Lajoie, *et al.*, Concordance between sites of tumor development in humans and in experimental animals for 111 agents that are carcinogenic to humans, *J. Toxicol. Environ. Health, Part B*, 2019, **22**, 203–236.

65 R. N. Sewduth and K. Georgelou, Relevance of Carcinogen-Induced Preclinical Cancer Models, *J. Xenobiot.*, 2024, **14**, 96–109.

66 V. F. Machado, M. R. Feitosa, J. J. R. da Rocha and O. Féres, A review of experimental models in colorectal carcinogenesis, *J. Coloproctol.*, 2016, **36**, 53–57.

67 Q. Zhao, L. Wang, R. Cheng, L. Mao, R. D. Arnold, E. W. Howerth, *et al.*, Magnetic nanoparticle-based hyperthermia for head & neck cancer in mouse models, *Theranostics*, 2012, **2**(1), 113–121.

68 S. R. C. M. Taboga, High Efficacy in Hyperthermia-associated with Polyphosphate Magnetic Nanoparticles for Oral Cancer Treatment, *J. Nanomed. Nanotechnol.*, 2014, **05**(03), 1000205.

69 C. J. Legge, H. E. Colley, M. A. Lawson and A. E. Rawlings, Targeted magnetic nanoparticle hyperthermia for the treatment of oral cancer, *J. Oral Pathol. Med.*, 2019, **48**(9), 803–809.

70 B. Yan, C. Liu, S. Wang, H. Li, J. Jiao, W. S. V. Lee, *et al.*, Magnetic hyperthermia induces effective and genuine immunogenic tumor cell death with respect to exogenous heating, *J. Mater. Chem. B*, 2022, **10**(28), 5364–5374.

71 K. Acikalin Coskun, M. Tutar, M. Al, A. G. Yurttas, C. Abay, N. Yurekli, *et al.*, Role of p53 in Human Cancers, Available from: https://www.intechopen.com/.

72 K. L. Yang, M. S. Chi, C. Y. Hao, H. L. Ko, Y. Y. Huang, R. H. Wu, *et al.*, Phase II clinical trial assessing the addition of hyperthermia to salvage concurrent chemoradiotherapy for unresectable recurrent head and neck cancer in previously irradiated patients, *Radiat. Oncol.*, 2025, **20**(1), 21.

73 K. Maier-Hauff, F. Ulrich, D. Nestler, H. Niehoff, P. Wust, B. Thiesen, *et al.*, Efficacy and safety of intratumoral thermotherapy using magnetic iron-oxide nanoparticles combined with external beam radiotherapy on patients with recurrent glioblastoma multiforme, *J. Neuro-Oncol.*, 2011, **103**(2), 317–324.

74 A. Nishikawa, Y. Suzuki, M. Kaneko and A. Ito, Combination of magnetic hyperthermia and immunomodulators to drive complete tumor regression of poorly immunogenic melanoma, *Cancer Immunol., Immunother.*, 2023, **72**(6), 1493–1504.

75 M. Ma, Y. Zhang, W. Yu, H. Y. Shen, H. Q. Zhang and N. Gu, Preparation and characterization of magnetite nanoparticles coated by amino silane, *Colloids Surf., A*, 2003, 219–226.

76 S. Slimani, C. Meneghini, M. Abdolrahimi, A. Talone, J. P. M. Murillo, G. Barucca, *et al.*, Spinel iron oxide by the co-precipitation method: Effect of the reaction atmosphere, *Appl. Sci.*, 2021, **11**(12), 5433.

77 S. Kacew and M. F. W. Festing, Role Of Rat Strain In The Differential Sensitivity To Pharmaceutical Agents And Naturally Occurring Substances, *J. Toxicol. Environ. Health*, 1996, **47**(1), 1.